

Field Mapping in Cyclotron Magnets

Timothy W. Koeth, James E. Krutzler
 Department of Physics and Astronomy
 Rutgers University, Piscataway, NJ, 08854

ABSTRACT A major educational component of the Rutgers 12-Inch Cyclotron is the design and testing of diverse magnetic field configurations [1]. Presently there are four pole tips in our repertoire which represent the most commonly encountered cyclotron fields: two azimuthally symmetric fields, and two azimuthally varying fields (AVF): one radial sector and one spiral sector. The azimuthally symmetric fields are used in weak focusing cyclotrons and synchrocyclotrons while the AVF fields are used for greater focusing in high intensity machines. AVF focusing of the 1950s made weak focusing obsolete, however recent developments in compact superconducting cyclotrons has revived its relevance. This paper describes measurement techniques and analysis experienced with the Rutgers 12-Inch cyclotron fields but is presented so as to assist others embarking on similar magnetic field measurements.

INTRODUCTION Two-dimensional (2-D) field mapping is necessary for computer model verification of, characterization of the magnet iron for, identification of field errors in, and subsequent confirmation of field “shimming” to cyclotron magnets. Further, visualizing the ruffled textures inherent to the azimuthal fields, these maps reinforce one’s intuition of beam orbit paths. Successful field mapping can produce some of the most exquisite images seen in accelerator physics.



Figure 1. Repertoire of pole tip configurations of the Rutgers 12-Inch Cyclotron.

The collection of pole tips used with the Rutgers 12-Inch cyclotron, displayed in figure 1, uniquely permits a comprehensive presentation of the measurement and analysis techniques associated with each of these field configurations while using a common set of measurement hardware. The influence and effects on the ion beam by each of these field shapes are discussed in several previous publications [2,3,4,5], while this paper specifically concentrates on the

measurements of the magnetic fields. Discussion of beam dynamics is only resorted to for comparison between the fields and their analysis. This paper will cover field mapping in an azimuthally symmetric field, typical of weak focusing cyclotrons and synchrocyclotrons, as well as azimuthally varying fields (AVF), including both radial and spiral sector fields. Although this discussion is set within the context of cyclotron fields, the following techniques are not strictly limited to cyclotron magnets; for instance a reader may find the following helpful in developing a measurement program for steering dipoles, spectrometer magnets, or analysis of nonlinear field components.

The magnetic fields in this paper will utilize both a 3-D Cartesian and cylindrical coordinate systems, switching between them as necessary. In the Cartesian and cylindrical coordinate systems the vertical component will be indicated as z , the “axial direction” which will be orthogonal to the plane of acceleration. The acceleration plane then will lie in the Cartesian $x-y$ plane or cylindrical $r-\theta$ plane. For our measurement apparatus it was natural to use a Cartesian grid, however, the authors have seen other cyclotron systems whose geometry made an automated $r-\theta$ platform preferable. For simplifying some of the following analysis we converted the measured data to polar coordinates.

While this paper gives details of our mapping apparatus, we do not suggest that readers develop a metrology program constrained by our specific equipment, but rather should consider

the higher level issues, and whenever practical, fit available tools to accomplish the necessary measurement. These issues can be broken down into seven discrete categories:

- Define the measurement region
- Develop measurement apparatus
- Alignment of measuring hardware
- Determine mechanical center
- Determine magnetic center
- Determine rotation (if necessary)
- Post-measurement analysis

APPARATUS. In all of the following examples, a standard, commercially available Hall effect Gaussmeter is used for the field measurements. The probe's 2-D positioning stage, shown in figure 2, was custom built to accommodate our magnet dimensions and ensure the necessary robustness for accuracy and reproducibility. The x - y stage was primarily constructed of aluminum with the exception of the T304 stainless steel 5/16-8 double lead (2 start) thread with 0.25-inch pitch. The lead screws of both x and y directions couple to the carriages by a two-part zero backlash nut. The lead screws are driven by Minebea's Astrosyn Type 23KM-K213-P7V stepper motors that advance 1.8 degrees per step. A ramp-up and ramp down of velocity prevents skipping. Since the load on the x - y stage is low, the stepper motors are only required to run at 25% their rated operating maximum current. The aggregate of lead screw pitch and motor resolution correlates to 800 steps per inch. To further minimize the potential for backlash, field measurements are only made while stages are moving in the "forward" direction.



Figure 2. Hall Probe based, X-Y field mapping apparatus on the Rutgers 12-Inch Cyclotron.

CONTROL & ACQUISITION The stage's stepper motors are controlled by two Automation Direct STP-DRV-4850 controllers, one dedicated to each axis. They are addressed through RS232 serial commands. Custom interface and control software was written by one of the authors. The software interface inputs

include desired x and y distance, step size, dwell time prior to measurement, and number of field measurements per position. At each measurement position the computer polls the Gaussmeter value via RS232. For ease and universality of post measurement analysis, data is written into a *comma separated variable* (.csv) file in either or both a list format, in which each measurement point data is appended to a row (this data can then be supplemented with other pertinent information, such as magnet current, temperature, etc.) and the second data format variant is a direct 2-D matrix, with each cell populated with the corresponding magnetic field value. The latter is convenient for fast plotting.

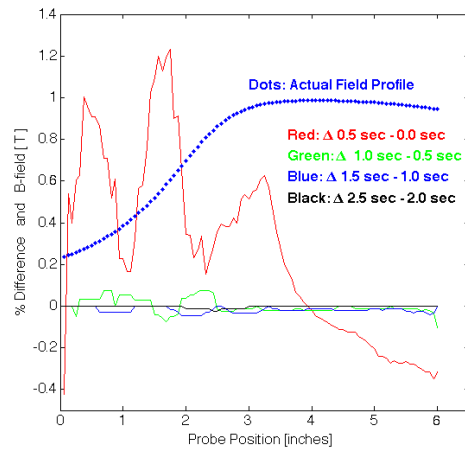


Figure 3. Percent difference between radial profile measurements of four dwell times. Actual field profile plotted (Blue dots) for reference.

A finite dwell time is required after each stage repositioning so as to allow any mechanical vibrations sufficient time to dampen out and to account for the Gaussmeter's response time. The meter's response time can be empirically determined through a sequence of identical measurements over a linear path through the largest field gradient experienced; incrementing the dwell time for each run. The optimal dwell time is determined by subtracting each profile's measurement from the subsequent profile until the fractional difference between profiles is comparable to stationary measurement noise. For the measurements in this report, the dwell time was determined by measuring the vertical field along a path with the greatest field change over the shortest distance of the radial sector AVF poletips. This was performed for ten dwell times ranging from the inherent latency of the system of about 0.7 seconds (zero dwell) to 5 seconds of dwell in half-second increments. The probe began approximately 3 inches outside of the magnet gap and entered a magnetic "hill" region as shown in figure 2. Profile differences

were determined for each dwell time pair, i.e 1.5-1.0 seconds and 2.0-1.5 seconds, etc. Four dwell time differences are plotted in figure 3, the actual field profile is also plotted for reference. There are field profile differences in excess of 1% between zero of half-second dwell times. However, there is no measurable difference between dwell times of 2.5 and 2.0 seconds. To be conservative, all field map dwell times were set to 3 seconds.

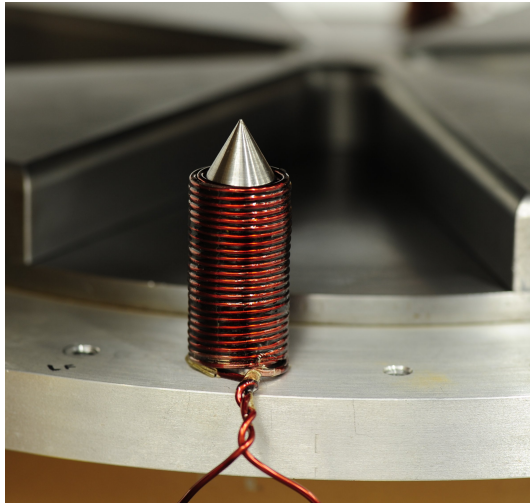


Figure 4. Iron needle to generate an alignment field bump.

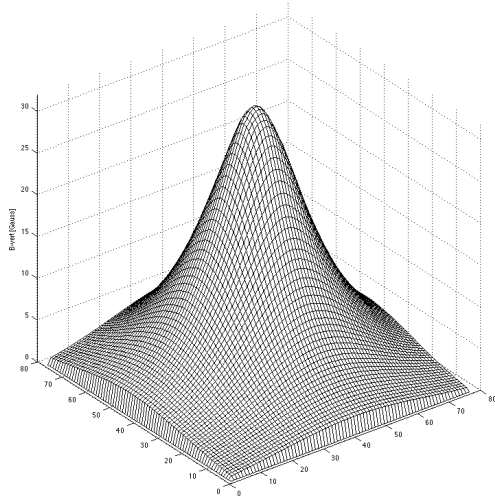


Figure 5. 2D map of single iron needle field bump.

ALIGNMENT Even with the greatest care during installation of the mapping hardware onto the cyclotron magnet, there will be alignment errors. These errors can be tolerated as long as the mechanical and magnetic centers can be located in the post measurement analysis. The magnetic field center may not share the magnet's mechanical center; therefore a method is also required to correlate a field map into physical space. Further accounting must be taken for rotational alignment, which is of special

importance in the non-azimuthally symmetric field configurations.

To calibrate the Hall probe's position against the magnet's mechanical center we have employed five field bumps that are formed by iron needles excited by small copper coils which are precisely located around the cyclotron magnet pole tips. An example is shown in figure 4. When energized, the needle's mechanical center creates a "field bump" whose peak precisely translates into the magnetic field space, displayed in figure 5. Further, a distribution of multiple field bumps can be used to confirm the translational calibration of the x - y stage motion.

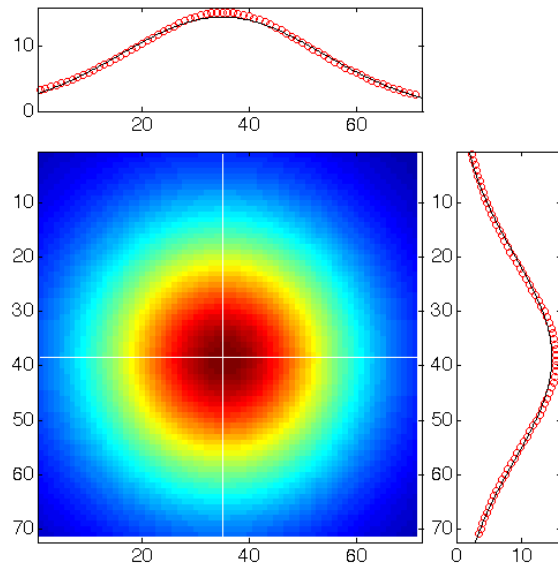


Figure 6. Fitting a 2-D Gaussian to profile to locate field bump centroid.

Because of the large difference in strengths, it was necessary for our field-bump calibration to be performed with the primary cyclotron magnet de-energized. After a full 2-D scan was completed; peaks, corresponding to the needles' centers are found by fitting a Gaussian, figure 6, to the measured field bump. Four needles were used to scale both dimensions; the fifth needle was used to break the symmetry, removing orientation ambiguities. Use of the lower field (<100 Gauss) bumps necessitates two scans - this then requires the assumption that the stage does not slip between scans. To gain confidence in this assumption, a dial indicator measured the distal placement of the probe carriage during 100 cycles of 15 1-inch travel increments in the forward direction followed by a single 15 inch return to "home". Home was a software defined location and not a hard physical limit. After 1600 travel manipulations were executed by 2.4 million motor steps, the probe carriage

reproducibly returned back to the distal point within the digital dial indicator's resolution of 0.0000 inches, as seen in figure 7.



Figure 7. Dial indicator reading 0.0000 inches after the 100th return of the probe carriage during a test run.

Figure 8 is an example of two field bumps captured within one map to calibrate the measurement increments against actual distance. Unfortunately, while the obvious codes for these analyses (in our case MatLab) provide appropriate tools they can also invert an axis, as demonstrated between figures 9 and 10, thus as a practical measure it was necessary to include the fifth field bump to account for these ambiguities. The five field bumps lie on a ## inch radius circle. In addition to identifying the x - y location of the field bump, any pair of field bumps can be used to calibrate the step-to-distance calibration. A post-measurement analysis of the two returned a distance of 2.500 inches while mechanical measurement found the distance to be 2.500. This was sufficient to rely on the step number-distance calibration.

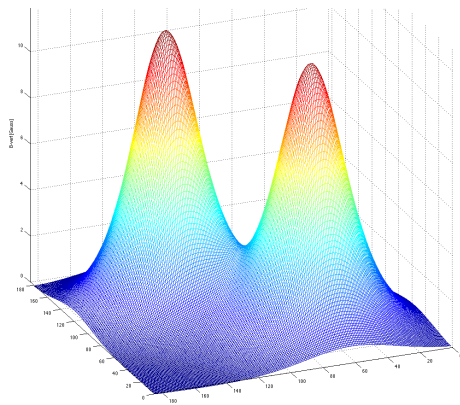


Figure 7. Test case of two field bumps to demonstrate distance calibration of the field mapping measurement system.

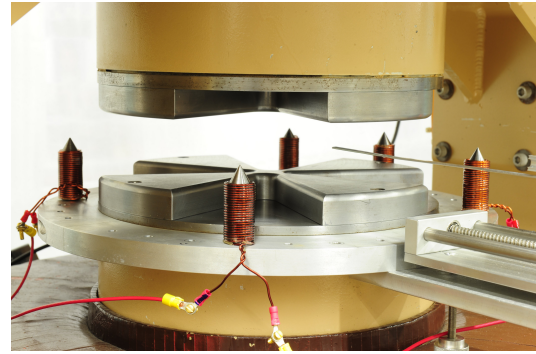


Figure 8. Measurement apparatus during field mapping of radial sector pole tips. Note the five field bumps installed about the periphery connected in series.

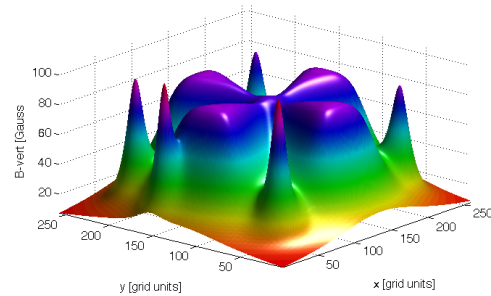


Figure 9. Although the 12-inch magnet was de-energized, residual magnetization was comparable to the field bump level.

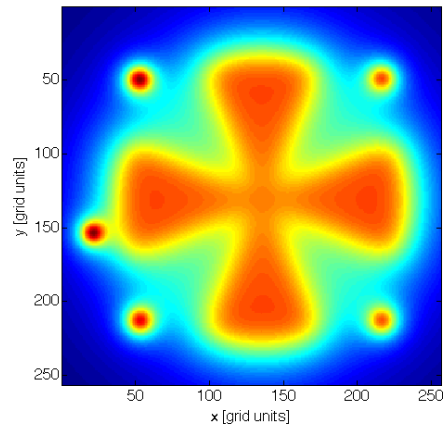


Figure 10. Same data as display in figure 9, but note apparent change of location of the 5th field bump - illustrating the need for the symmetry-breaking marker.

Field Mapping a Weak Focusing Magnet

Finding the magnetic center of a 2-D azimuthally symmetric (weak focusing) field map, such as displayed in figure 11, is straightforward. The procedure starts by drawing a reference circle on the field map that must contain the field's center, but which is not necessarily concentric with it. Then plot B_z along this reference circle. If the centers are concentric, the field will be constant along the circumference; however, if they are not concentric, the magnetic field values will vary around the circular path. Such field plots along the entire azimuth will display a sinusoidal

variation. It is evident from figure 12 that the magnetic center is within the bounding circle, but not concentric with it. The averaged B_z of each measurement circle is also plotted in figure 12 as a red line. The five radii plotted show the average vertical field drop-off with radius necessitated by the focusing gradient.

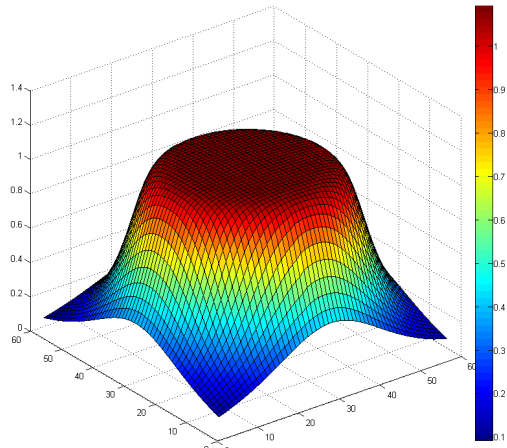


Figure 11. B_z 2-D field map of the weak focusing pole tips.

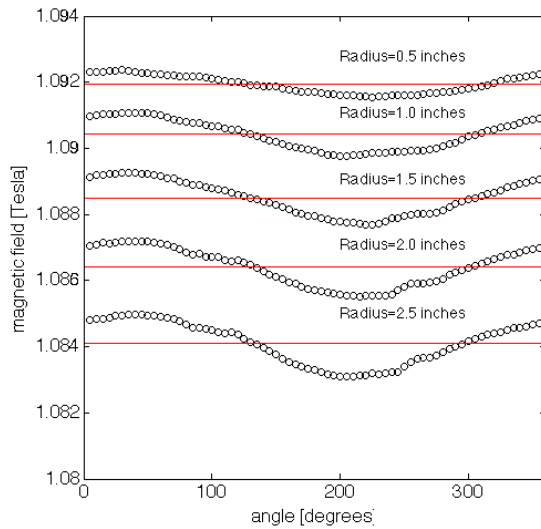


Figure 12. Plotting B_z as a function of azimuth at several radii before locating the center – the circles are the data points, the red lines are the average B_z values.

We now can determine the magnet center by sweeping the center of the reference circle first in the x and then the y directions. The standard deviation of the values about the reference circle were calculated, stored and plotted - an example sweep of the x direction is depicted by red dots in figure 13. After a sweep in x , which included the magnet center, the sequence of standard deviations was fit to a parabola from which the minimum standard deviation, *i.e.* the center locations, could be inferred also shown in figure 13. With the x -center value in hand, this is

repeated in the y -direction to similarly locate the y -center. This process was reiterated until the variation in the determinable center was comparable to the variation in the measured data. To demonstrate the effectiveness of this technique, the field is now plotted along concentric circular paths for same five radii about the fitted center, figure 14. Again, the average field is plotted as a red line.

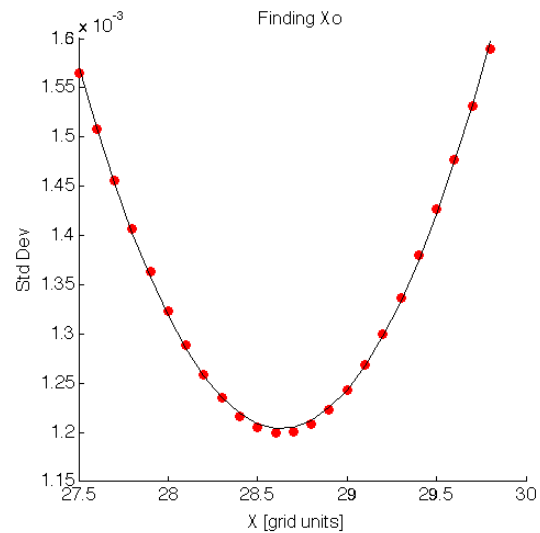


Figure 13. The magnetic center at a single radial location was found by locating the minimum standard deviation of the B_z values for a sweep of reference circle's center in x (and y).

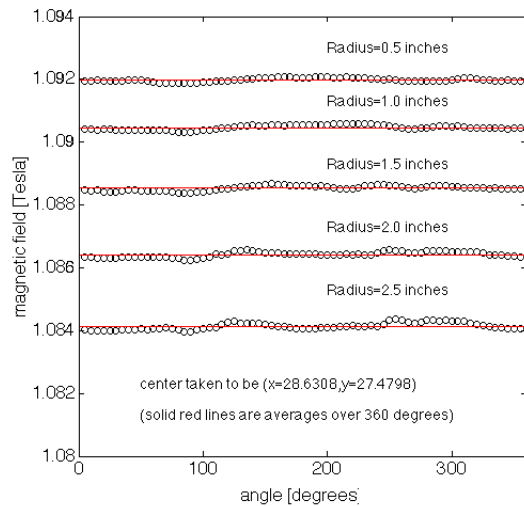


Figure 14. Plotting B_z as a function of azimuth at several radii after locating the magnetic center.

It is interesting to compare the evaluated centers for each radii so as to determine the level to which the overall field is axis-symmetric. In this particular case, the centers of each measurement circle were found to be coincident to 10^{-4} .

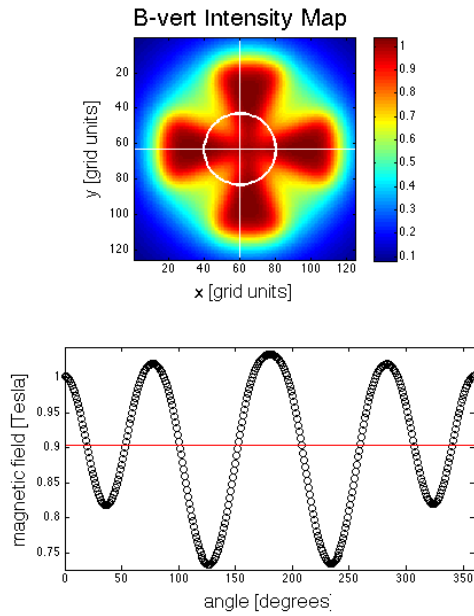


Figure 15. Upper images reference circle location on the full 2D field map. Lower plots B-field along analysis reference circle, distortion indicating non-concentric centers.

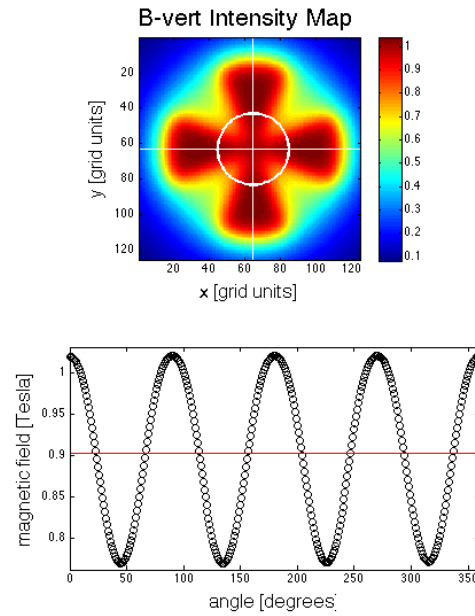


Figure 16. Upper images reference circle location on the full 2-D field map. Lower plots B_z -field along analysis reference circle.

Field Mapping a Radial AVF Finding the center of square-wave stepped radial- or spiral-sector AVF fields requires more sophistication than that of the weak focusing field. Once the center is found, the resulting map can be ported into equilibrium orbit codes, or otherwise used in post-measurement field characterizations. We again start by defining a large reference circle that clearly encompasses the field's center. For example, in the upper portion of figure 15, we choose a reference circle to have a radius half that of the maximum ion radius - in our case 2.5 inches or 20 grid units. Plotting the magnetic field along the circular path will reveal the undulating hills and valleys. A plot of B_z along a reference circle that is non-concentric will produce a distorted and asymmetric waveform, as shown in the lower portion of figure 15.

The nearer the center of the reference circle is to the actual field center, the more the waveform will display a repetitive trace of N-fold symmetry, where N is the number of hill-valley pairs. The lower portion of figure 16 displays a near pure sinusoid. Defining the circumference of the reference circle to be the fundamental wavelength, we perform a fast Fourier transform (FFT) on the field data. As the reference circle and the magnetic field centers become coincident, the Nth harmonic will be maximized, while the second, and others will be minimized.

For illustration, this analysis is performed on the measured field map of Rutgers 12-Inch Cyclotron fitted with the set of radial sector azimuthal field poletips. Since it has four-fold periodicity of hills and valleys the reference circle is swept to maximize the 4th harmonic, while minimizing the second, third, and fifth. A routine was written in MatLab to iteratively step the reference circle along a line that is parallel to one axis, i.e. taking the x-axis to begin with. Note this does not require the circle sweep to be on the axis, just along a line that is parallel to one of the "defined" axes even if there is a rotation error; this will still identify the center of the axis being swept. Although the 4th harmonic peaks while the others harmonics are *minimized*, they do not go to zero; this is a consequence of sweeping off of the orthogonal axis' zero crossing. Figure 17 shows the FFT evaluation of 30 reference circle sweep with the 4th harmonic maximized near x grid unit 136. A derivative of a polynomial fit to the 4th harmonic yields the true x-center value, shown in left plot of figure 19. Now that the center along the x-axis is identified, the routine is updated with that value and an identical sweep is performed in the y-axis direction. Since positioned at the previously identified x=0, the crossing of y=0 will bring all the undesired harmonics near to zero as observed in figure 18. This procedure was reiterated until the variation in the determinable center was comparable to the variation in the measured data.

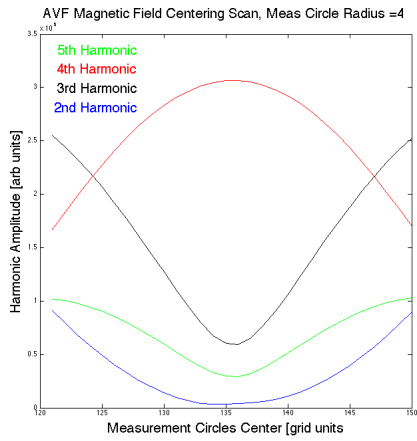


Figure 17. Harmonic strengths after 30 scans in the x direction. Note that while 2nd, 3rd, and 5th harmonics minimize, they do not zero.

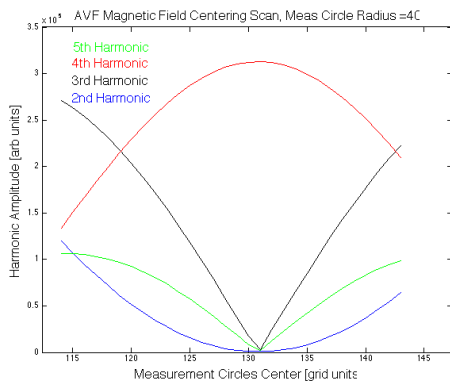


Figure 18. Harmonic strengths after 30 scans in y direction. Note, since scan is performed on x -center, 2nd, 3rd, and 5th harmonics do zero at minimum.

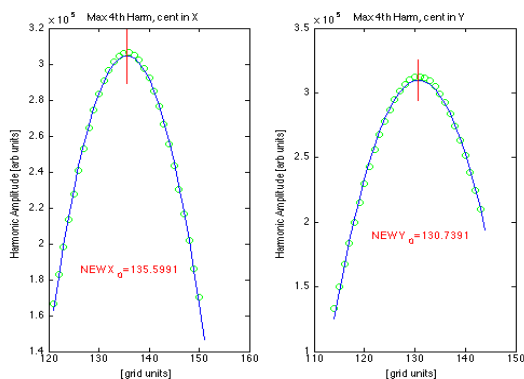


Figure 19. Fits to 4th harmonic signal from scans in x and y for a single reference circle. Their peaks are taken as the x and y centers respectively.

After another polynomial fit, now to the y -FFT data, and derivative thereof to locate the maximum of the 4th harmonic the right portion of figure 19 can be completed. This center locating process can be repeated for reference circles of multiple radii to evaluate the amount the magnetic centers wander and determine the

impact those errors will have on the beam's orbit. Figure 20 plots the "wandering" centers for reference circles of radius 24 to 80 grid units (or 1.5 to 5 inches).

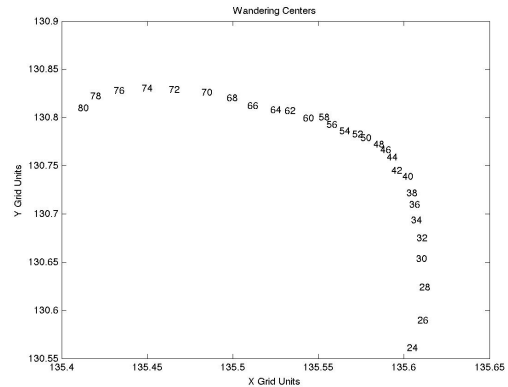


Figure 20. Display of the reference circles' centers wandering. The corresponding circle is noted by the numerical value of the data markers. 1 grid unit = 1/16 inch.

Once centers have been obtained, further analyses of the field map to determine relevant criteria of the aggregate magnetic field, such as average azimuthal field as a function of radius and the field index, flutter, and axial tune. An example of this analysis is shown in figure 21 for the radial sector poletips.

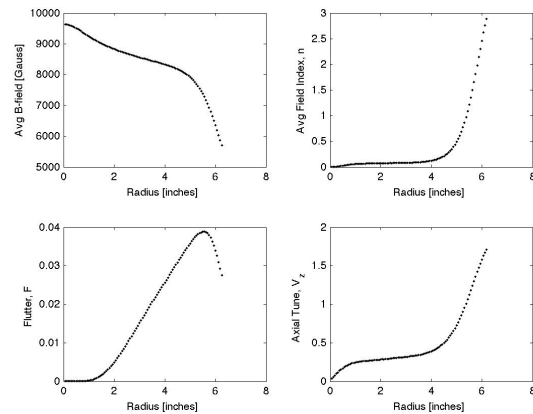


Figure 21. Average field, average field index, flutter, and axial tuned determined from the 2-D field map analysis.

Field Mapping Spiral Sector AVF We simply extend the AVF analysis to include the flutter-field phase advance with radius for our spiral sector AVF fields. Note, this is valid for symmetric spiral field such as our AKG270 Archimedean spiral pole tips. Additionally, rotational alignment errors become pronounced in AVF fields of particularly aggressive spiral angles. This is of primary importance when comparing with the simulated field. It should be noted that this rotational analysis and correction could be applied to radial sector fields if required.

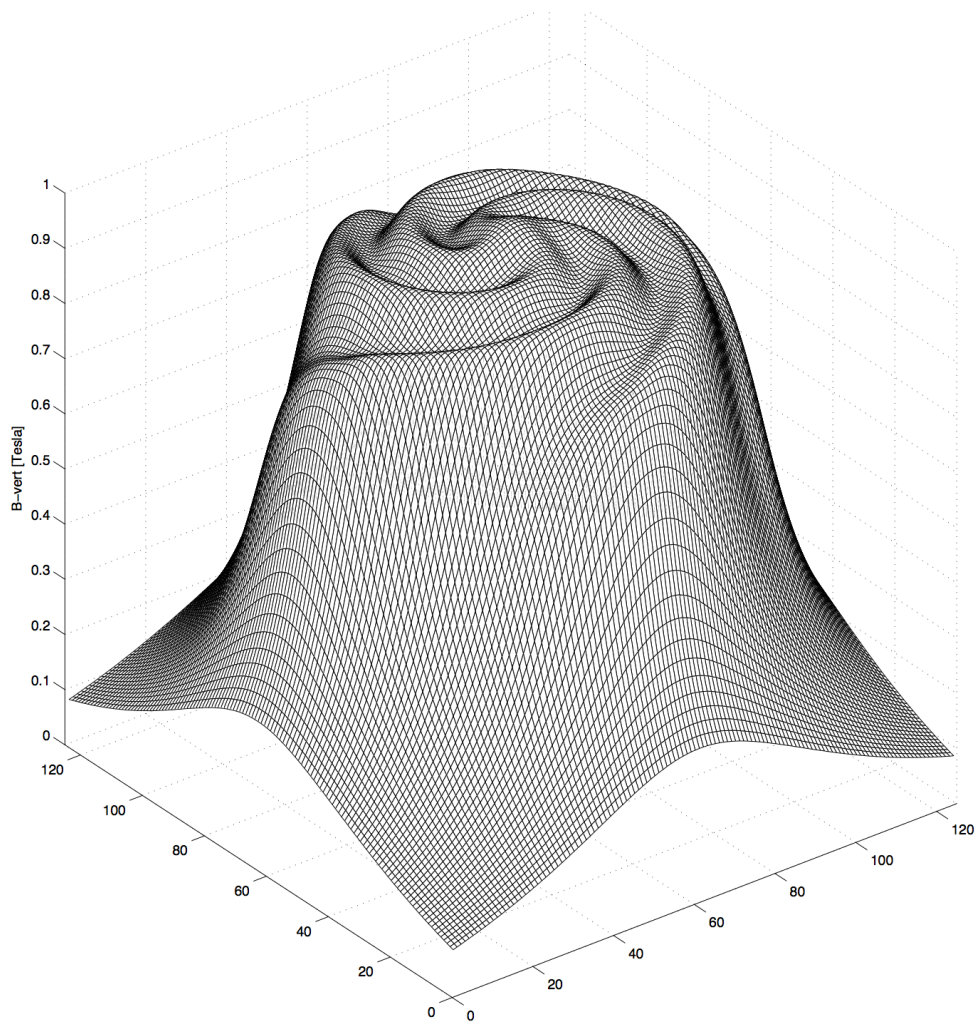


Figure 23. Measured field map of AKG270 Azimuthally Varying Field configuration on the Rutgers 12-Inch Cyclotron.

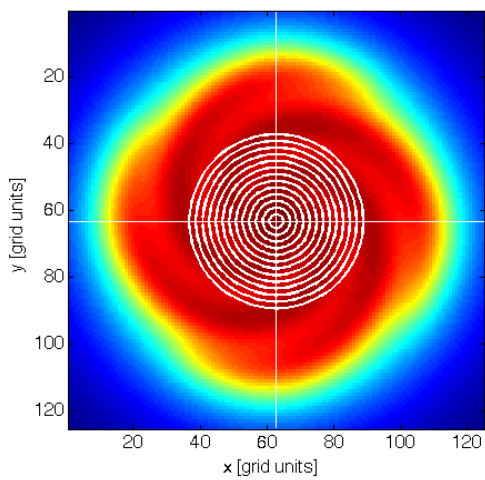


Figure 24. Illustration of multiple reference measurement circles in the spiral sector AVF poletip analysis. The corresponding field values along each circle are plotted in figure 25.

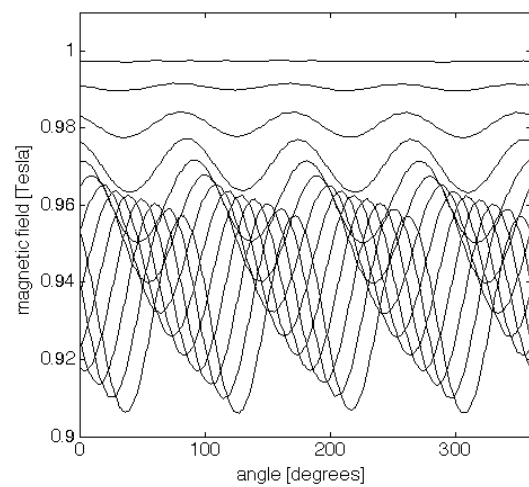


Figure 25. Magnetic field plotted along circumference of 13 reference circles shown in figure 23. They demonstrate the initial constant central field dropping into the AVF field, the phase shift depicting the pitch of the spiral sectors.

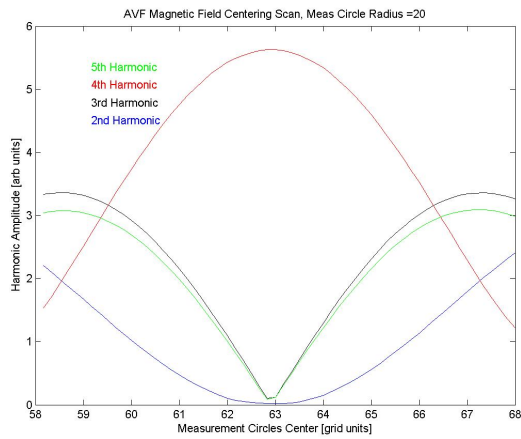


Figure 26. Resulting FFT of 2nd, 3rd, 4th, and 5th Harmonics. The magnet center resides where the 4th is maximized and the others are minimized.

Our example utilizes the “AKG270” pole tips that are a 4-fold AVF configuration employing an Archimedean spiral through 270 degrees from center to periphery. The FFT based analysis is used to locate the magnet center on the field map of figure 23, in which the central region of this field starts as an abrupt weak-focusing field before transitioning into the AVF splines. Figures 24 and 25 demonstrate the flutter’s phase advance with radius leading to the spiral’s edge focusing.

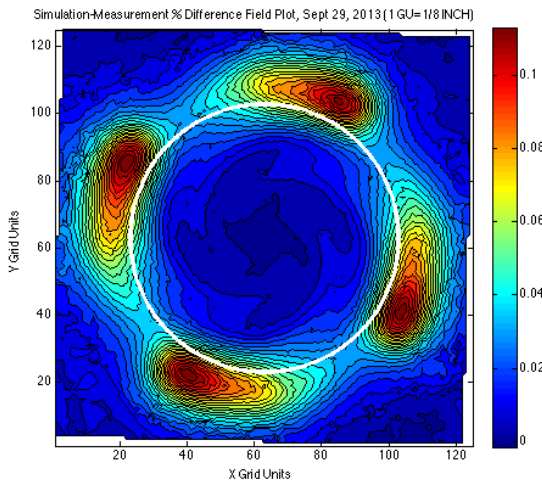


Figure 27. Post-rotation fractional difference between simulation and measurement of the AKG270 spiral poletips. The white circle indicates maximum ion radius of 5 inches.

After the FFT process finds the location of the magnet center in the field map, as shown in figure 26, it is necessary to rotate the field map to make the final assessment between the measurement and simulation. A MatLab routine has been developed to simply rotate the measured data set about the analyzed center so as to minimize the *rms* difference between it and

the simulation, the final rotational of 1.4 degrees is shown in figure 27.

BENCHMARKING Finally, to confirm the calculations of the field map analysis, we present the comprehensive comparison between measured and simulated field maps processed with our MatLab analysis tools (AVF Analysis Modules I & II), and those outcomes against a PIC simulation. The comparison between a measured and generated 2-D field map verifies the magnet model simulation, while the comparison with the PIC simulation ensures that the physics is captured in the MatLab analysis of the 2-D map. The Simion simulation tracks the progression of the ions undergoing the collective effects in the 3-D field to provide “independent” values for the average magnetic field, field index, and axial tune. The simulated magnetic field volume is generated by a 3-D E&M solver, which exports the field components B_x , B_y , B_z in a 231x231x53 unit array of 1 mm spacing in each direction. This volume is then imported into PIC Simion where ions are flow with orbits of realistic displacements and their trajectories tracked. The B_z field component of the 27th layer from the simulated 3-D volume was extracted to form the “simulated” 2-D field map of 231x231 grid points. Hence the comparison is not truly independent in that the Simion simulation and simulated field map utilize the same magnet model, but their approaches are independent.

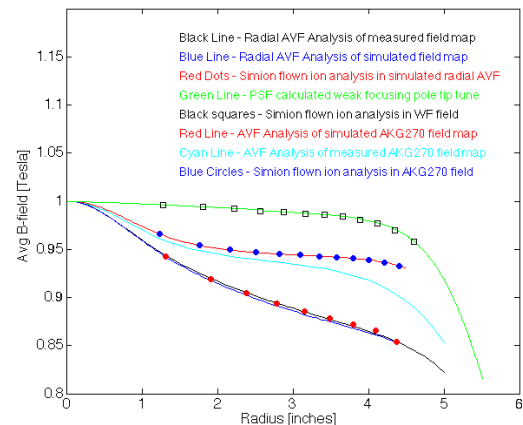


Figure 28. Average fields as a function of radius for weak focusing, radial and spiral sector AVF poles

A comparison was performed for three of the four sets of pole tips shown in figure 1; namely the “good” weak focusing, radial sector, and spiral sector field configurations. The Simion simulations were performed at nominally 10 discrete energies starting at 50 keV and incrementing by 50 keV until the limiting field boundary was encountered.

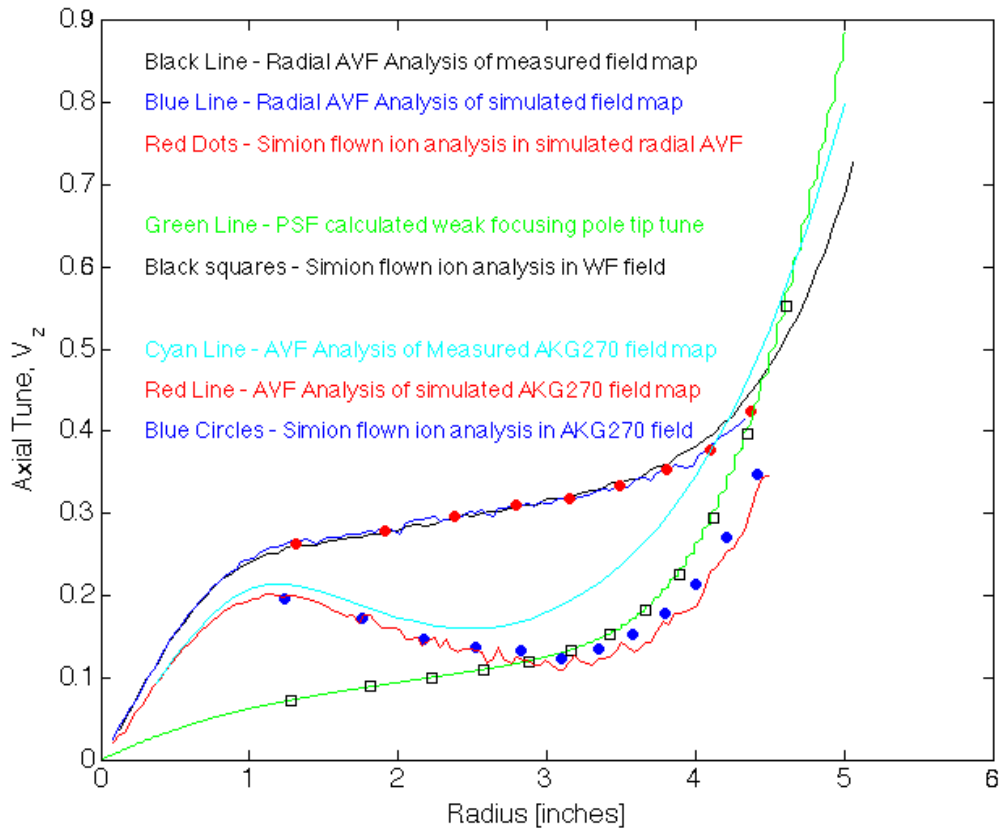


Figure 29. Axial tune calculated from measured and simulated field maps as well as determined by Simion for all three fields types: weak focusing, radial sector AVF and spiral sector AVF on the Rutgers 12-Inch Cyclotron.

The average fields for each case, normalized to 1-Tesla at $r=0$, is plotted as a function of radius in figure 25. There is overall agreement between measurement and simulation of the WF and Radial sector fields, and greatest discrepancy at large radius of the spiral sector field – this is most likely due to the saturation of the narrow vanes of the measured spiral sectors. The average field in this limited energy regime (600 keV maximum) is a direct measurement of the Rutgers 12-Inch Cyclotron’s isochronism. At this point obtaining the average field from a 2-D map is trivial; the average field that an ion has experienced in Simion is inferred from the period of revolution from the cyclotron equation:

$$f = qB / 2\pi m$$

Where f is the ion’s revolution frequency, q is its charge, and m is its mass and B is the average magnetic field it traverses. The weak focusing field possesses the flattest average field profile, while the radial sector poletips have the greatest average falloff - so great that it amounts to be an unusable field. The spiral sector AVF field is a compromise between the two. Next, figure 29, compares the axial tune, V_z , a standard metric of

focusing strength [6]. The tune can be calculated from the field map by:

$$V_z^2 \approx n + F^2(N^2/N^2 - 1)$$

Where n is the average field index, F is the flutter, and N is the periodicity of the AVF field.

The weak focusing poletips live up to their name, while the radial sector shows almost triple the focusing strength. Again, the spiral sector tips meet the two extremes half way with a combined practical average field profile and an increased focusing strength during the early turns.

Obviously these two metrics, average field and axial tune, guide the design of cyclotron magnets. Because of the agreement shown between the analysis of the measured and simulated fields and their successful benchmark against Simion, this analysis approach can be used to quickly assess a field during design, relegating the laborious task of phase space mapping and determining the limits of stability to the few the final contenders.

ACKNOWLEDGEMENTS. The authors would like to acknowledge the Rutgers Physics Machine Shop for their support in making and remaking our x - y mapping stage. We thank Rutgers' Educational Physics Fund for financial support and the University of Maryland's Institute for Research in Electronics and Applied Physics for support through equipment loans.

REFERENCES

[1] Koeth, T.W., *Undergraduate Education With the Rutgers 12-Inch Cyclotron*, **Physics Procedia**, Volume 66, 2015, Pages 622–631

[2]http://www.physics.rutgers.edu/cyclotron/papers/Betatron_Studies.pdf

[3]http://www.physics.rutgers.edu/cyclotron/papers/AVF_study_Dec_31_2011.pdf

[4]http://www.physics.rutgers.edu/cyclotron/papers/12_inch_magnet_studies_4.pdf

[5] Koeth, T.W., *Beam Physics Demonstrations with the Rutgers 12-Inch Cyclotron*. Cyclotrons13, WEPPT025, Vancouver, British Columbia, Canada. 2013

[6] J.J. Livingood, "Principles of Cyclic Particle Accelerators," D. Van Nostrand, 1961